Flight Control System Design for a High Altitude, Long Endurance Airplane: Sensor Distribution and Flexible Modes Control

Hamidreza Bolandhemmat*

***Abstract*— This manuscript outlines the control system design process for a solar-powered unmanned high-altitude long endurance flying wing aircraft, called Aquila, which was developed by the Facebook Connectivity Lab to serve as communication backhaul for remote and rural connectivity. With 400kg mass and 42m wing-span, it was designed to autonomously fly at stratospheric altitudes of the atmosphere between 18 and 26km for months at a time.**

I. INTRODUCTION

Performance of the solar-powered High-Altitude Long Endurance (HALE) aircrafts in closing the energy cycle on winter solstice days could be notably enhanced by increasing the aspect-ratio[1] (L/D>35) and decreasing the weight. Both, however, contribute to higher structural flexibility and thereby existence of lightly damped "coupled" rigid body and elastic modes which could result in adverse Aeroservoelastic (ASE) phenomena such as Limit Cycle Oscillations (LCO), and (body-freedom) flutter. LCO is used to describe sustained, periodic, but not catastrophically divergent aeroelastic motions. It results from a nonlinear coupling of aircraft structural response and the unsteady aerodynamics. Flutter is characterized by an unstable interaction between the elastic modes and the unsteady aerodynamic loading. The ASE phenomena are usually excited by either control surface actuations or by the atmospheric disturbances at critical dynamic pressures. If not controlled effectively, both can cause structural failures leading to loss of the aircraft.

In the conventional flight control design philosophy, aircraft is considered to be a lumped mass in the air with only 6 Degree of Freedom (DOF) motion variables being the rigid-body modes. These modes are measured by installing an IMU inside the fuselage. However, due to their light weight and high aspect-ratio wing and fuselage, the HALE airplanes[2] behave as multi-body dynamic systems comprised of distributed lumped masses which are connected with aeroelastic spring and dampers. Therefore, a distributed sensing and control design methodology must be pursued to measure and control the rigid body and elastic modes, simultaneously. In other words, with increasing the aircraft structural flexibility, the elastic modes vibrate at frequencies much closer to the rigid body modes and therefore must be considered in the control system design process. Figure 1 compares the Aquila aircraft jig-shape with the deformed shape under the first symmetric bending elastic mode oscillating at below 1Hz.

Figure 1: The undefomed Aquila airplane shape (gray) is compared to the deformed shape under the first symmteric bending and torsion elastic modes (coloured as function of the deformation magnitude); Left picture portrayes the front view while the right shows the side view.

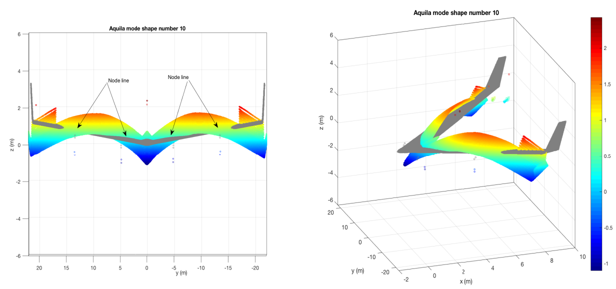

This article aims at demonstrating such a methodology in the design of flight control and active flutter suppression systems for the Aquila aircraft. Challenges in specifying effective sensor and servo placements on the aircraft to provide sufficient observability and controllability of the prevalent under-damped elastic modes are also addressed. In order to reduce complexity, and increase the design transparency, the classical frequency loop-shaping techniques are adopted[3]. Other design techniques including OBLTR, and MIDAAS are explored in references [1]. Both techniques utilize feedbacks only from the output measurements. OBLTR is an LQG/LTR based method with adaptive terms to account for the modeling uncertainties, whereas MIDAAS is LQR based with an optimal output blend to isolate and suppress the problematic elastic mode(s).

This manuscript is organized as follows. Section II presents characteristics of the Aquila's open loop flight dynamics across its flight envelope. Section III deals with the sensing and actuation system design for the Aquila control. The control requirements are given in Section IV. Section V covers design of the primary flight control laws for the rigid body modes control. Section VI reviews design of an active flutter suppression control laws for the elastic modes control. The Gust Load Alleviation (GLA) control loop is presented in Section VII.

II. OPEN LOOP FLIGHT DYNAMICS ANALYSIS

Aquila is a 400kg, unmanned backward sweep flying-wing aircraft with 42m wingspan. More than half of the aircraft weight is devoted to batteries to store the solar energy

*Research Scientist at Facebook Connectivity Lab (hbolandhemmat@fb.com).

[1] Induced drag is inversely proportional to span.

[2] The next generation of the passenger aircrafts and cargo transports are also designed with slender high aspect ratio wings, and therefore a similar flight control design philosophy must be considered.

[3] The corresponding design toolbox can be found @ FBHALEControl.

throughout the day for the night flight. The aircraft is powered by four electric motors and propellers[4] mounted under the wings. The motors differential thrust is also utilized to control the aircraft in the roll and yaw channels. Figure 2 illustrates the Aquila configuration[5].

Figure 2: Aquila unmanned aircraft configuration.

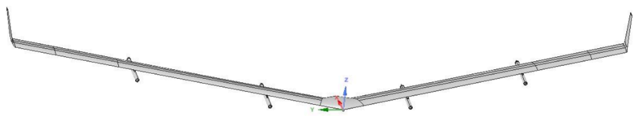

Spoilers are mounted to effectively control the rate of descent of the aircraft during the approach and landing. They are also deployed when the motors differential thrust authority drops under a threshold. To enhance the aircraft directional stability, the aircraft is equipped with winglets. The longitudinal pitch channel is controlled by approx. 2m-long elevon control surfaces installed at the end of each wing. The elevons can also move differentially to assist in controlling the roll and yaw motions. Their travel range is limited to a specified range. Bandwidth of the elevon servo actuators is 3Hz (-3dB). Note that the roll control authority is limited due to the high aerodynamic roll damping

The aircraft flight envelope covers altitudes of up to 28km, with a low Equivalent Airspeed (EAS) range of 9 to 15m/s (dynamic pressure range of between 50 to 110 Pa). However, speeds above 12m/s are within the flutter boundary at higher altitudes (>7km). The nominal (weight dependent) stall speed is at 8.5m/s EAS.

The aircraft structure is modeled by using the shell and beam finite element models. The aerodynamic behavior is captured by using the Doublet-Lattice aerodynamic models. The Blade Element Theory is utilized to model the propulsion system thrust and torque at various flight conditions. The resultant model used for the control laws design consists of 112 states which includes the aeroelasticity effects of the flexible structure and aero-lags of the unsteady flow. The nonlinear model is trimmed and linearized at various flight conditions across the flight envelope. The linearized models are then used for the open loop flight dynamics analyses and the control system design. A summary of the modal analysis depicting the interconnections between the states and various modes, the eigen vectors, are given in the next subsection.

A. Modal analysis

Eigenstructure analyses are carried out to determine interconnection between the states, each degree of freedom and various dynamic modes. This is necessary to determine the relative significance of the rigid body and elastic degrees of freedom which is helpful for the (flutter) control system design and sensor selection. The preliminary analysis is performed by using the aircraft full-order model at 10m/s and sea level. As illustrated in Figure 3, the aircraft has a slightly unstable Spiral (S) mode with a time constant larger than a minute. The Dutch Roll (DR) mode frequency is low and close to the Phugoid (Ph) frequency at roughly 0.45rad/sec. This is mostly due to the large roll stability coefficient (c_{ℓ_p}), and similar inertia properties around the x and z body axes ($I_{xx} \cong I_{zz} \cong 47000$ kg.m^2). As a result, these modes can interact at non-zero bank flight conditions.

Figure 3: Unstable spiral (S), Dutch-Roll (DR) and Phugoid (Ph) modes at 10m/s and sea level.

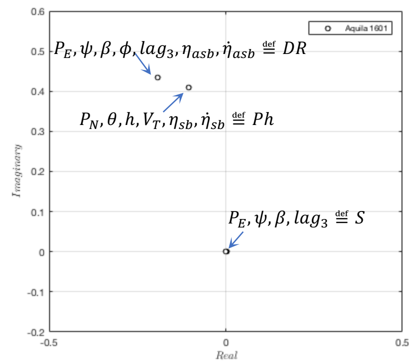

Figure 4 shows an *elastic* Short Period (eSP) mode at 5rad/s. This mode consists of a conventional Short Period mode coupled with the first symmetric bending and torsion degrees of freedom[6] represented by the generalized modal states $\eta_{sb}, \dot{\eta}_{sb}$ and $\dot{\eta}_{st}$, respectively. There is another coupled elastic and rigid body mode at 6.5rad/s which is mostly dominated by the first asymmetric bending and torsion degrees of freedom.

Figure 4: The elastic Short Period (eSP), first asymmetric bending (ASB) mode, Plunge and pitch ($Pl + \theta$), and Roll (R) modes at 10m/s and sea level.

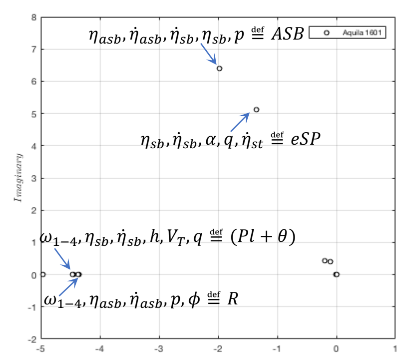

The first few elastic degrees of freedom of the aircraft including the symmetric bending and torsion are given by Figure 5.

[4] The propellers can be unidirectional without any significant adverse effect from the P-factor (asymmetric disc effect) and the gyroscopic moment. The blade pitch angles can be also controlled to control the glide slope angle.

[5] Note that the Center of Gravity (CG) is not on the airplane ($x_{CG} \cong 4m$ aft measured from the nose).

[6] An indication that the rigid body and elastic modes are coupled.

Figure 5: 1st symmetric bending (right), first asymmetric bending (left), 2nd symmetric bending (bottom left) and first symmetric torsion (bottom right) degrees of freedom in-vacuo.

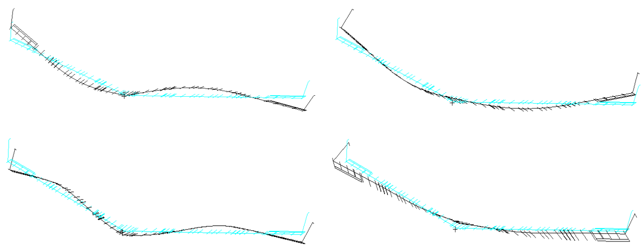

Note that to determine the relative significance of the states, the unitless modal states must be replaced by new states with physical units [2], [3]. These new states are comprised of the angular displacements and rates as measured on the deformed aircraft.

Figure 6: Phasor diagram for the eigen vector associated with the elastic short period mode indicating a coupled rigid body and elastic mode.

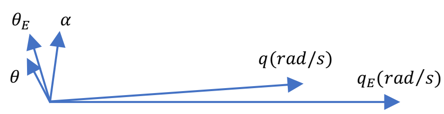

Figure 6 depicts the phasor diagram associated with the elastic Short Period mode in which q_E and θ_E are the new pitch attitude and rate states measured on the deformed aircraft at the IMU sensor location. The IMU location node is shown in Figure 7 (x_{IMU} ≅0.4m aft from the nose of the aircraft). Also, Figure 1 provides visualization of this mode shape.

Figure 7: Location of the analysis nodes/sensors identified by the light brown diamonds distributed the aircraft wing/body.

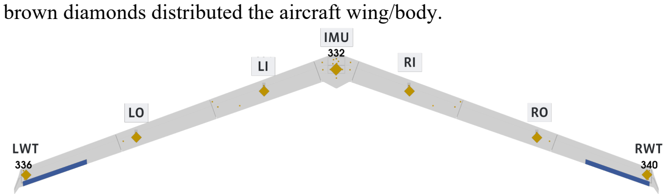

The original rigid body states including α, q, and θ are measured on the undeformed aircraft (i.e., the body mean axis). The phasor diagram is obtained from a simplified reduced order model where the inertial position states were truncated, and the aerodynamic lags were residualized. It illuminates the significant contribution of the center body pitch rate, q_E, due to the elastic degree of freedom, $\dot{\eta}_{sb}$.

The aircraft dynamic behavior varies with variations of the speed and altitude. This can be seen in the frequency response plots of the θ_E/δ_e system at 12.5m/s EAS in Figure 8. It's illustrated that damping and frequency of the Phugoid and elastic Short Period dynamic modes are approximately halved by only 6km of altitude increase. The mode variations over the entire altitude range are displayed in Figure 9 and Figure 10 for the two speeds of 10m/s and 12.5m/s EAS, respectively. Again, it is evident that the damping and frequency of the modes are decreased as altitude increases. For the 10m/s EAS case, the Dutch Roll mode becomes slightly unstable as altitude increases beyond 20km. For the 12.5m/s EAS case, the elastic Short Period mode becomes unstable once the altitude exceeds the 16km range resulting in a Body Freedom Flutter (BFF).

Figure 8: Frequency responses of the θ_E/δ_e transfer function over 6km altitude increase at EAS=12.5m/s.

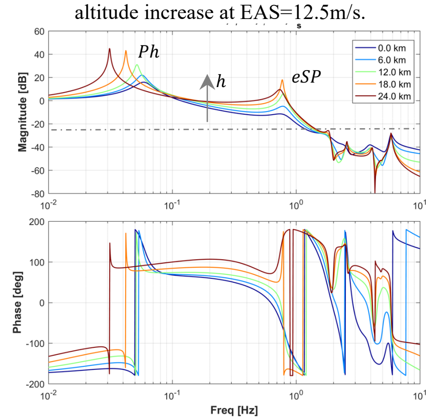

Figure 9: Variation of the (aeroelastic) modes with altitude at EAS=10m/s

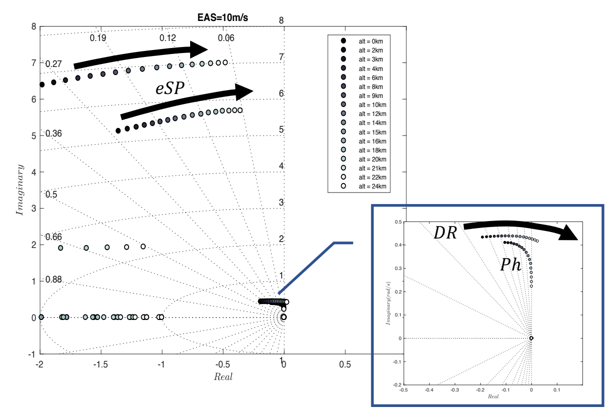

Figure 10: Variation of the (aeroelastic) mode with altitude at EAS=12.5m/s

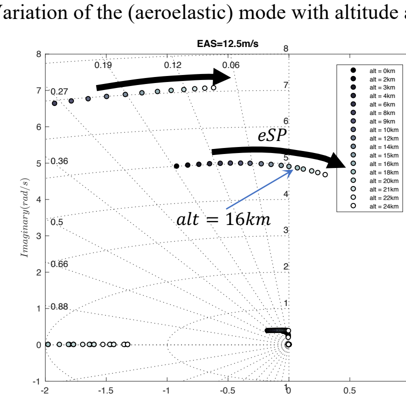

Further analysis revealed that the altitude onset of the BFF is reduced to 8km as speed increases to 14.72 m/s EAS. Results of the Aquila dynamic modes stability analysis is summarized in Figure 11. The dotted line represents the flutter boundary[7]. Analysis of this section justifies the requirement for control laws with adjustable gains and parameters to account for the variations in the aircraft dynamic response.

Figure 11: Aquila's dynamic modes stability boundary.

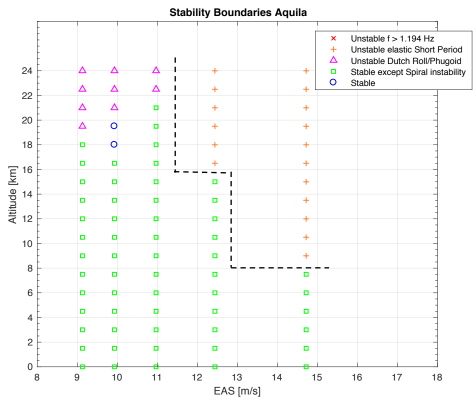

III. Distributed Sensing and Actuation System Design

To measure linear and angular motion of the aircraft, a GPS aided inertial navigation system incorporating an IMU[8] at the center body (the IMU location node) is utilized. The system measurements provide sufficient information for controlling the six rigid body degrees of freedom of the aircraft. To suppress the BFF, the first symmetric bending degree of freedom which plays a significant role in shaping the elastic Short Period dynamic mode must be controlled; and therefore, must be measured. Observability and impulse residue analyses are adopted to determine sensors type and configuration providing the richest information for the feedback loop. The modal impulse residue metric associated with the kth mode from the jth input to the ith output is given by [3],

$$R_{i,j,k} = (c_i^T v_k)\,(\mu_k^T b_j) \tag{1}$$

Where b_j and c_i^T are the corresponding column and row of the input and output matrices to the jth input and ith output, respectively. v_k is the kth column of the right eigen vector matrix and μ_k^T is the kth row of the its inverse (for Hermitian matrices the left eigen vector matrix).

Table 1 summarizes the analysis results for the first symmetric bending degree of freedom and the elevon-normal acceleration input-output pairs. These results are obtained by using the aircraft model within the flutter region at 18km and 12.5m/s EAS. Four different accelerometer sensor locations are examined including the Right Inner (RI) motor pod, Right Outer (RO) motor pod, and the Right Winglet nodes. The node locations are depicted in Figure 7. It's demonstrated that mounting the accelerometers at the wingtip nodes provide the largest degree of observability and impulse residue metrics for the elastic degree of freedom. The results obtained for the gyroscopes at similar locations are not comparable.

Table 1: Modal Controllability, Observability and Impulse residue metrics for the first symmetric bending DOF, and elevon-normal acceleration input-output pairs.

MODE	***OBSV***	***CTRB***	***IMPULSE RESIDUE (m/s²)***
$(N_z, \delta_e)\vert_{IMU}$	1.00	51.38	51.69
$(N_z, \delta_e)\vert_{RI}$	1.06	51.38	54.54
$(N_z, \delta_e)\vert_{RO}$	1.27	51.38	65.36
$(N_z, \delta_e)\vert_{RWT}$	1.61	51.38	82.92

Next, the root locus analysis is performed to evaluate the flutter control design complexity by using the averaged wingtip accelerometers feedback. The number of unstable branches in the root locus plot is considered as a metric for the control design complexity; The more unstable branches in the root locus plot, the higher the order of the compensator must be. Figure 12 indicates that there are three unstable branches for the feedback loop using the wingtip accelerometers. Further analysis revealed that the number of unstable branches drops to only one when accelerometers mounted at the inner motor pod locations are utilized. This is illustrated in Figure 13.

Figure 12: Root locus plot for the transfer function from the elevon to the averaged normal accelerations from the wingtips accelerometers.

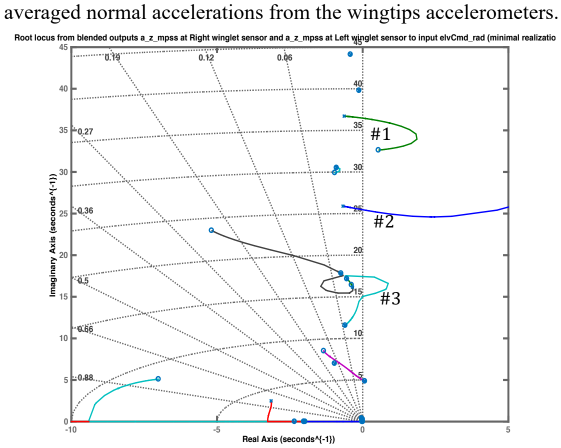

Figure 13: root locus plot for the transfer function from the elevon to the averaged normal accelerations from the inner motor pods accelerometers.

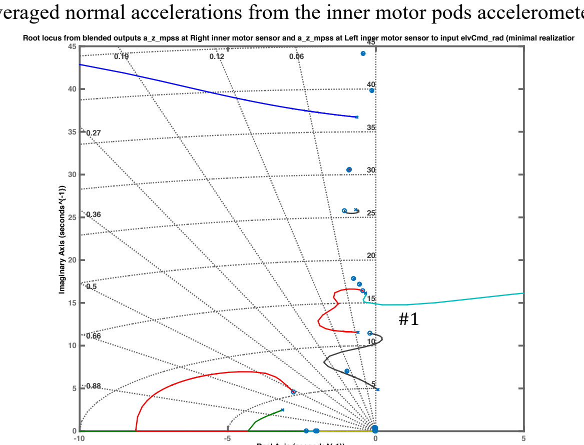

[7] Note that Ground Vibration Testing (GVT) is usually required to validate the structural dynamic modes on the ground and therefore the flutter boundary. The flutter boundary is sensitive to the mass and mass distribution.

[8] An IMU consists of a triad of gyroscopes and triad of accelerometers.

To reduce the unstable branches, the system zeros must be correctly placed. This could be done by blending the accelerometers signal from the inner motor pod nodes into the signals from the wingtip accelerometers[9]. The distributed sensing system consisting of the four vertical accelerometers are then utilized for the flutter suppression. Note that the left and right accelerometer signals are averaged to remove effects of the asymmetric bending degree of freedom.

As explained in section II, Aquila's primary flight control surfaces include the collective elevon for the pitch control and the differential elevon and differential motors for the roll and yaw/heading control. Although, the collective elevon can be utilized in the flutter control loop, adding a separate flutter control surface prevents the undesired couplings between the channels. The optimal location(s) of the flutter control surfaces can be identified by using conventional techniques such as ILAF[10] or based on the Controllability analysis. For the Controllability analysis the input matrix needs to be reconstructed based on the mode shapes at provisional servo locations as below

$$B_{n\times m} = \begin{bmatrix} B_{rb} \\ 0_{1\times m} \\ \phi_1^T \\ \vdots \\ 0_{1\times m} \\ \phi_{n_q}^T \end{bmatrix} \tag{2}$$

Where m is the number of servos, n_q is the number of elastic degrees of freedom, and ϕ_k^T is the kth row of the mode shape matrix Φ defined by

$$\Phi_{n_q\times m} = \left[\Psi_{1_{n_q\times 6}} \quad \cdots \quad \Psi_{p_{n_q\times 6}} \right] \tag{3}$$

The kth elastic degree of freedom is controllable from a specific servo/control surface location if and only if the following conditions are satisfied [2]:

1. There is at least one nonzero entry in the row matrix ϕ_k^T ,
2. If there are ν elastic modes with the natural frequency f_n, the corresponding ϕ_k^T's form a linearly independent set.

The analysis recommends mounting extra collective control surfaces at the entire trailing edge of the center body or at the root of the wing for effective suppression of the BFF mode. Next section outlines the control system requirements followed by a brief design review.

IV. Flight Control System Requirements

The flight control system is required to provide pitch, speed, altitude, climb rate, and heading tracking and hold modes. Each mode control loop is required to retain stability margins of at least 6dB in gain (gain margin) and 30deg in phase (phase margin). Desired bandwidth of each control loop is given in Table 2. The bandwidths are defined such that the aircraft level mission/ station keeping requirements are satisfied. Note that the closed loop bandwidth requirements are translated into the open loop gain crossover frequency requirements. To provide satisfactory load disturbance rejection and command tracking, magnitude of the open loop gain must be larger than $20dB$ at the low frequency region ($\leq 0.1\omega_{gc}$); while it must be smaller than -$20dB$ at the high frequency region ($\geq 10\omega_{gc}$) to avoid amplifying the atmospheric gusts and measurement noises. To provide satisfactory robustness to modeling uncertainties, the maximum values of the Sensitivity (S) function and its complementary (T) must not exceed $4dB$. This is crucial for the sensitivity functions measured at the plant inputs specifically in the frequency region where the gust PSD is still substantial ($\omega_g \leq 6$ rad/s).

TABLE 2: BANDWIDTH OF THE PRIMARY FLIGHT CONTROL LOOPS

CONTROL LOOP	**ω_b(rad/s)**
PITCH ATTITUDE LOOP	0.5
TAS LOOP	0.1
ALTITUDE LOOP	0.1
VERTICAL VELOCITY LOOP	0.2
HEADING LOOP	0.15

The closed loop damping of the augmented modes are desired to exceed 0.1, with the exception to the Spiral mode which is desired to become neutrally stable. Finally, the maximum load factor across the aircraft wingspan must not exceed 1.3g.

V. Primary (Rigid Body Modes) Flight Control Laws Design

Primary flight control laws are constructed based on the successive loop closure technique. This allows for considering effects of the windup and the rate/magnitude saturation limiters of each nested loop in the design. The full coupled aeroelastic model of the aircraft is utilized to account for the elastic and rigid body modes, simultaneously[11]. Also, the model incorporates the servos and propulsion system dynamics.

Each nested control loop comprises at least one lead/lag (PD/PI) compensator and one roll-off filter with adjustable gains and coefficients. MATLAB's systune function is used for tuning the adjustable parameters such that the time and frequency domain design requirements are satisfied. First, the requirements are converted into infinity-norm and 2-norm cost functions. For example, the frequency domain loop shaping requirement is converted into the following infinity-norm cost function (loop shaping cost function):

$$J_{ls}(k_c) = \left\| \begin{matrix} W_s S(k_c) \\ W_T T(k_c) \end{matrix} \right\|_\infty \tag{4}$$

Where W_s and W_T are some frequency weighting functions (filters) derived from the desired loop shapes. The time domain

[9] The weight penalty for adding the four accelerometers and the required wiring harnesses was 750gr (26awg with 3.5gr/ft mass density).

[10] Identically Located Acceleration and Force

[11] Note that asymmetricity in mass and stiffness distributions of the left and right wings results in coupling of the longitudinal and lateral modes.

reference tracking requirement is converted into a 2-norm cost function given by Equation (5):

$$J_{rt}(k_c) = \|\tfrac{1}{s}(T(k_c) - T_{ref})\|_2 \tag{5}$$

In which T_{ref} is the reference model closed loop transfer function. In both cost functions, the adjustable gains and coefficients are concatenated into the optimization vector k_c. Next, a local minima solution is computed by the non-smooth optimization routines within the systune function [5].

To accommodate the variations of the aircraft dynamics behavior across the flight envelop (see Section II), the control gains and coefficients are scheduled based on nonlinear functions of dynamic pressure ($\bar{q}$) and altitude (h) as below:

$$k_c = k_c(\bar{q}, h, \bar{q}h) \tag{6}$$

As a result, outcome of the optimization routine involves coefficients of the nonlinear scheduling function given by the Equation (6). The next two subsections briefly review the autopilot structure and present the results.

A. Longitudinal Modes Control

The longitudinal autopilot consists of the airspeed, and altitude tracking and hold modes as outer loops. The control loops are configured based on the total energy rate control technique. Their outputs include pitch attitude, climb rate and power commands for the inner loops. In this technique, pitch attitude and thrust are controlled simultaneously to alleviate the inherent couplings between the airspeed and altitude modes. In addition, the pitch attitude control loop takes advantage of a pitch damper to enhance the aircraft pitch dynamic stability behavior (c_{m_q}). Figure 14 displays the structure of the pitch damper incorporating a lead compensator with k_q, and (q_n, q_d) as adjustable gain and coefficients, respectively. The damper also includes a bandpass filter to notch out effects of the higher frequency elastic mode at around 25rad/s.

Figure 14: Structure of the pitch damper (most inner) control loop.

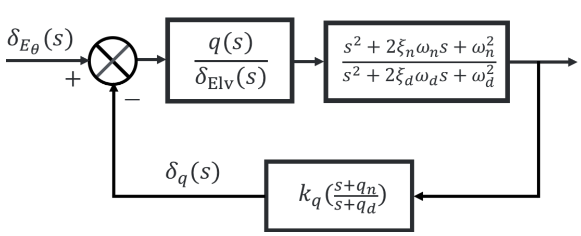

Tuning results for the numerator and denominator coefficients, (q_n, q_d), of the lead compensator are shown in Figure 15 for the low altitude portion of the flight envelope. Figure 16 provides a comparison between the design requirements and the time and frequency responses of the tuned pitch attitude control loop. The top window of the Figure 16 plots the tuned system loop gains (the blue curves) against the desired frequency response (the dotted dash line). It is demonstrated that the frequency response requirements are met for all the flight conditions across the envelop; The pitch attitude tracking performance against the reference model time response is illustrated in the second window. And finally, the third window shows that the phase and gain stability margin requirements are all satisfied.

Figure 15: Tuned coefficients of the pitch damper lead compensator.

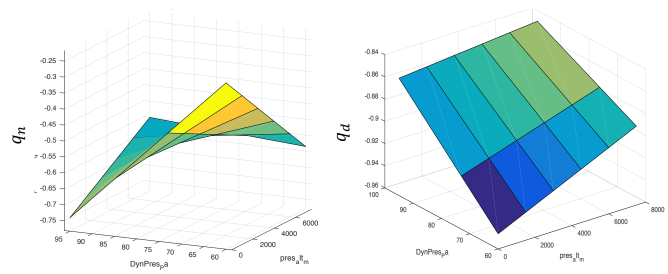

Figure 16: Comparison of the time and frequency design requirements against the actual responses of the pitch attitude inner loop across the flight envelop.

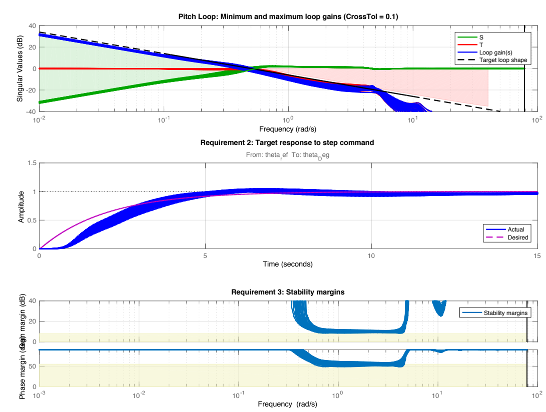

The comparison between the design requirements and the tuned airspeed loop responses in the time and frequency domain is provided by Figure 17.

Figure 17: Comparison of the time and frequency design requirements against the actual responses of the airspeed outer loop across the flight envelop.

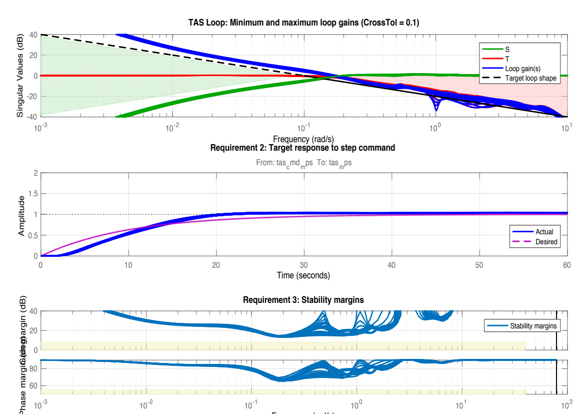

B. Lateral-Directional Modes Control

The lateral-directional autopilot consists of the heading (ground track) tracking and hold mode as the outer loop. Outputs of this loop include the bank attitude, and the yaw rate commands to the inner loops. The bank attitude and the yaw rate commands are kinematically related by the coordinated turn formula as shown in Figure 18[12].

Figure 18: Structure of the yaw rate inner control loop

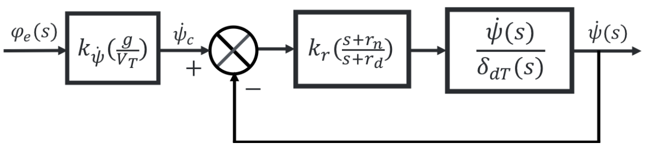

To avoid the unstable Spiral mode, change of the heading of the aircraft is mostly performed by yawing and not rolling. The roll attitude authority is limited to ±5deg soft and ±10deg hard limits. The differential thrust has sufficient effectiveness on both the yaw and roll (due to the large c_{l_β}) channels. This can be realized by comparing the open loop frequency responses of the differential thrust (δ_{dT}) and differential elevon (δ_{dElv}) to the aircraft roll attitude in Figure 19.

Figure 19: open loop frequency responses of the differential thrust to the roll attitude ($\frac{\varphi}{\delta_{dT}}$) and from differential elevon to the roll attitude ($\frac{\varphi}{\delta_{dElv}}$). Units of the transfer functions are in degrees.

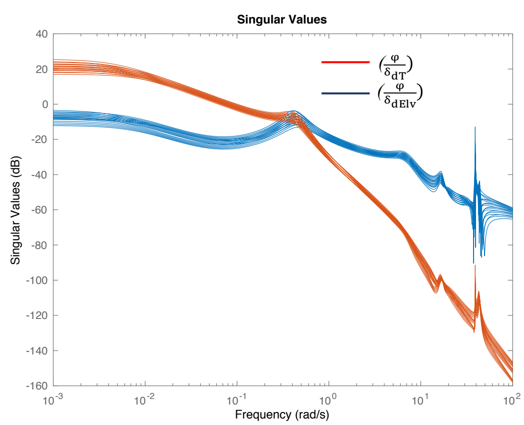

However, spiral divergence is still a concern for the large-wingspan, slow-flying Aquila because even a small yaw rate results in a large airspeed gradient across the span. This airspeed gradient causes reduction in lift on the inside wing of a turn and strong yaw-roll coupling that can lead to a divergent spiral. As a result, during an established turn, the differential elevons are deflected in the opposite direction of the turn to counteract the loss of the lift on the inside wing. At the high bank attitude trim angles (≥ 5deg), the differential thrust is also commanded in the opposite direction of the turn to counteract the lift reduction and to arrest the roll.

Figure 20 compares the performance of the tuned yaw rate inner loop against the desired time and frequency requirements. Design of the active flutter suppression control laws is presented next in Section VI.

Figure 20: Comparison of the design requirements against the actual time and frequency responses of the yaw rate inner loop.

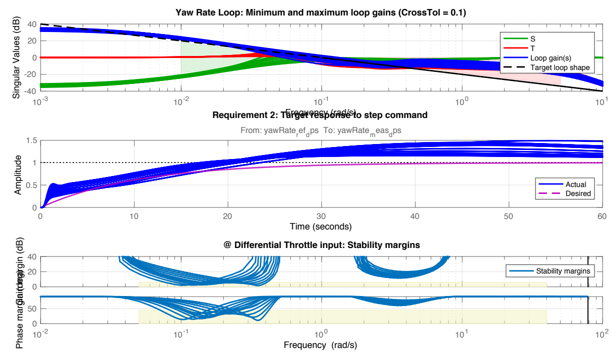

VI. ACTIVE FLUTTER SUPPRESSION (FLEXIBLE MODE CONTROL) LAWS DESIGN

As described by the modal analysis in Section II, the genesis of the body freedom flutter is the elastic Short Period dynamic mode which becomes unstable across the dotted-line depicted in Figure 11. The onset of the flutter instability is predicted to be at 12.5m/s EAS at 16km altitude; hence, the aircraft linearized model at this flight condition is utilized for the control laws design. The flutter control loop constructs the most inner loop of the longitudinal autopilot. Analysis of Section III revealed that the most effective control surface combination consists of the collective elevons and additional collective surfaces near the center body. However, in this study only the collective elevons are deployed. Structure of the control loop is depicted in Figure 21 where the loop control surface command is augmented to the surface demand from the primary (rigid body) autopilot mode. Also, the most effective sensing system is determined to consist of four accelerometers distributed on the wings at the left and right inner motor pods and at the wingtips. Therefore, a blended accelerometers feedback is utilized for the control design as given by Equation (7)[13]:

$$\frac{N_z}{\delta_e}|_{\text{Blended}} = \frac{1}{2}\left(\frac{N_z}{\delta_e}|_{\text{LI}} + \frac{N_z}{\delta_e}|_{\text{RI}}\right) + \frac{1}{2}\left(\frac{N_z}{\delta_e}|_{\text{LWT}} + \frac{N_z}{\delta_e}|_{\text{RWT}}\right) \tag{7}$$

Note that the left and right accelerometer measurements are averaged to remove effects of the asymmetric elastic modes which are negligible in the flutter mode.

Figure 21: Structure of the body freedom flutter mode control loop.

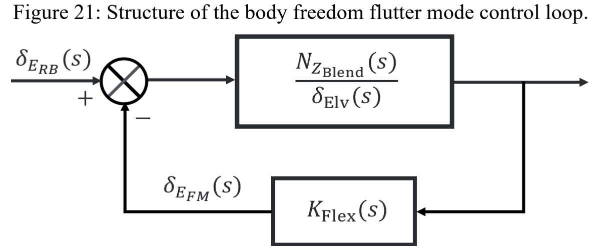

The control design requirements include the stability margins of 30deg phase margin (PM), and 6dB gain margin

[12] Note that to have the coordinated turn formula held accurate for the HALE aircrafts, the effective bank attitude must be used which might be different than the bank attitude measured by the centerbody IMU.

[13] If the phase delay between the right and left wingtips deflection during the turn maneuvers is high, an outer control loop must be devised based on the wingtip gyros to maintain the aircraft shape during the maneuvers.

(GM). The controller $K_{Flex}(s)$ is then comprised of a lead compensator to add phase and a notch compensator to provide gain at the right frequencies. Since the unstable elastic Short Period mode is located at ω_f=4.9rad/s, the lead compensator is configured to provide at least 30deg phase margin around this frequency. Then, the notch center frequency is placed at the ω_{-180° frequency to provide the required gain margin. The controller structure is given by Equation (8),

$$K_{Flex} = 0.05\left(\frac{s+2.7}{s+12.4}\right)\left(\frac{s^2+2(0.2)(15.7)+(15.7)^2}{s^2+2(0.6)(15.7)+(15.7)^2}\right)\left(\frac{50}{s+50}\right)\ \frac{rad}{m.s^2} \qquad (8)$$

where a roll-off filter with the cut-off frequency at 50rad/s is also included to improve the high frequency response characteristics. Figure 22 illustrates the closed loop system performance in the frequency domain. It is shown that a PM of 39.6deg at 6 rad/sec and a GM of 8.18 dB at 25.6rad/s is maintained. An airspeed tracking performance beyond the flutter boundary with all the loops closed is illustrated in Figure 23.

Figure 22: Performance of the designed flutter control loop.

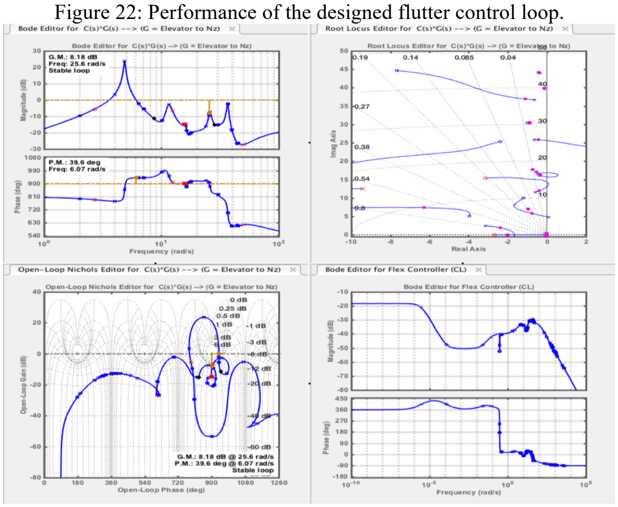

Figure 23: Speed tracking performance with all the autopilot loops closed.

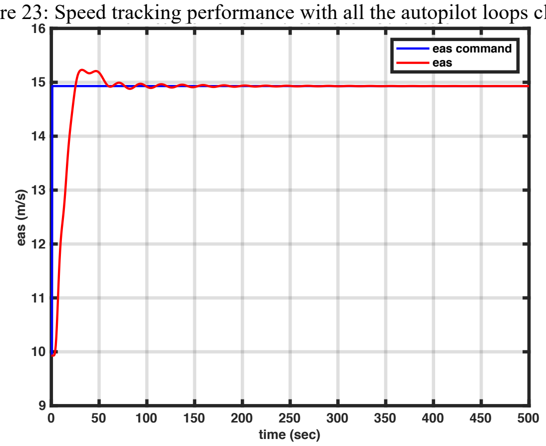

VII. GLA Control Loop Design

The GLA control loop becomes active once any of the distributed accelerometers (including the center body IMU) measures a local dynamic load of larger than 1.15g. Then, the control loop deploys the spoilers for lift dumping and the load alleviation. The loop structure is shown in Figure 24. The controller $K_{GLA}(s)$ is comprised of a simple gain and a lag filter shown by Equation (9):

$$K_{GLA} = 0.02\left(\frac{12}{s+12}\right)\ \frac{rad}{m.s^2} \qquad (9)$$

which is designed to mitigate effects of the vertical gust to the normal acceleration (specific load) output. Figure 25 illustrates the GLA loop effectiveness by comparing the frequency responses from the vertical gust to the normal acceleration for two cases of with (blue) and without (red) the GLA loop.

Figure 24: Structure of the GLA control loop.

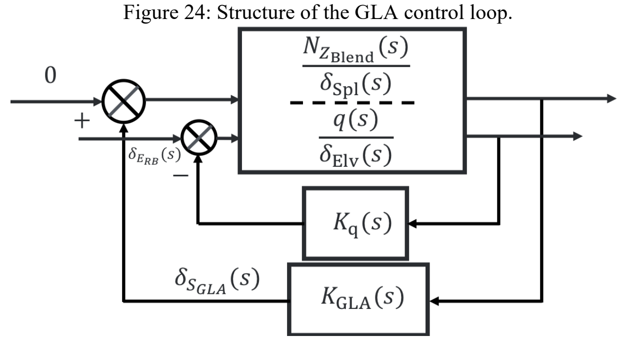

Figure 25: frequency responses of the normal acceleration to the vertical gust with and without the GLA loop.

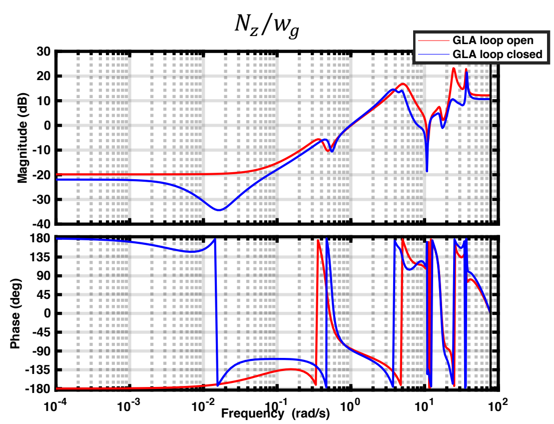

Acknowledgment

Author would like to thank Prof. Dave Schmidt, Abe Martin, David Flamholz, David Liu, Joe Robinson, Kevin Roughen, Ben Thomsen, Martin Gomez, Vishvas Suryakumar, Ajay Modha, Andy Cox, Iman Alizadeh, Jack Marriott, Anthony Pham, Dr. Anuradha Annaswamy, Dr. Eugene Lavrestsky, Dr. Brian Danowsky, Dr. Peter Seiler for help, support and valuable technical consults.

References

[1] Z. Qu, B. Thomsen, A. M. Annaswamy, and E. Lavrestky "An Adaptive Controller for Very Flexible Aircraft," AIAA Guidance, Navigation and Control Conference, 2013, Boston, USA.

[2] D. Schmidt, Modern Flight Dynamics. McGraw-Hills, 2012.

[3] M. V. Cook, Flight Dynamics Principles, A linear systems approach to aircraft stability and control. Elsevier Aerospace Engineering Series, Third Edition, 2013.

[4] D. Schmidt, "Stability Augmentation and Active Flutter Suppression of a Flexible Flying-Wing Drone," Journal of Guidance, Control, and Dynamics, 2016, Vol. 39, No. 3.

[5] P. Apkarian, D. Noll, "The H_∞ Control Problem is Solved," AerospaceLab Journal, Issue 13, Sep 2017.